2011

Bone Tissue Quality Determination of Mice Through a Novel Reference Point Indentation Technique

Matin Lendhey
CUNY City College

Bone Tissue Quality Determination of Mice Through a Novel Reference Point Indentation Technique

---

Thesis

Submitted in partial fulfillment of
the requirement for the degree

Master of Science (Biomedical Engineering)

At

The City College of New York

Of the

City University of New York

By

Matin Lendhey

May 2011

Approved:

_____

Professor Mitchell Schaffler, Thesis Advisor

_____

Professor John Tarbell, Chairman
Department of Biomedical Engineering

Table of Contents

List of Figures and Tables

Abstract

Bone strength deteriorates with age; which increases the susceptibility to fracture. Current clinical techniques for the estimation of bone strength are largely Bone Mineral Density (BMD) based. However, toughness, which is the ability to resist crack growth, plays a critical role in bones' fracture resistance. Traditionally, toughness measurements involve large samples, obviating their use clinically. Recent data suggest that a reference point indentation approach provides a novel, localized measure of toughness from whole bones. In the current research, we evaluated the sensitivity of this method to discriminate small known differences in fracture toughness that exist between inbred mouse strains with genetically based differences in mineralization. To achieve this we measured a new parameter called Indentation Distance Increase (IDI) which has been shown to be related to fracture toughness. We also analyzed associated microdamage patterns and the surrounding tissue microarchitecture. In addition, Tissue Mineral Density (TMD) was measured and analyzed. IDI was highest in AJ mice followed by C3H and B6 and a similar pattern was found for TMD. These data precisely parallel previously reported phenotypes for bone brittleness. Crack formation occurred under the indenter tip, suggesting that the tip acts as an "opening-wedge". These cracks initiated in the transverse direction and were then diverted into the longitudinal direction. Other toughening mechanisms were also observed: un-cracked ligament bridging was present in C3H bones, while B6 femurs showed extensive delamination, consistent with internal slippage in the mineralized collagen fibrils. These data suggest that the reference point indentation is a suitable and sufficiently sensitive method for detecting differences in brittleness as a result of small differences in mineralization. This may have important clinical implications in the assessment of fracture risk.

Introduction

Bone is an extraordinary and adaptable material which is in a continual state of remodeling which allows it to conform to its function [1]. It is a type of dense connective tissue that supports and protects various organs of the body, acts as a source of red and white blood cells and stores minerals such as calcium and phosphorous. Bone has a very complex hierarchical structure, so an understanding of how microscopic structural features combine to affect macroscopic properties, is therefore very important [2]. Bone is initially laid down as a protein phase which is primarily composed of tropocollagen molecule - collagen type I. Each molecule is built from three polypeptide chains arranged in a triple helical geometry and stabilized by hydrogen bonds between different amino acids (Figure 1). This soft collagen phase gives bone its elasticity and ability to dissipate energy under mechanical loading. Staggered arrays of tropocollagen molecules form collagen fibrils, which themselves arrange into arrays to form collagen fibers. Tiny hydroxyapatite crystals form between collagen fibrils gap, which mineralize as bone grows and mature (Figure 1). Collagen fibers then arrange into parallel or tilted bundles which are further organized at microstructural scales into a lamellar structure with adjacent lamellae 3-7 μm thick [3].

Lamellae are produced in different conformations in different bone types, perhaps the most commonly seen is the cylindrical structure called the osteon. This is the characteristic feature of cortical bone. Cortical bone constitutes about 80% of skeletal mass, forms dense protective shell and is present around all bones beneath the periosteum, primarily in the shaft of long bones. It has porosity of 5-10%. It allows slow circulation of nutrients and withstands greater stresses [1].

The elastic modulus and ultimate strength of cortical bone in tension are 11-19GPa and 107-146MPa, respectively and in compression are 15-20GPa and 156-212MPa, respectively [4].

Trabecular bone makes up 20% of the skeleton and is a highly porous rigid lattice like structure designed mainly for high strength along with low mass and its spaces are filled with marrow. It is present in vertebrae, flat bones and in the ends of the long bones. It allows diffusion of nutrients and waste between blood vessels and cells and withstands greater strain [1]. The elastic modulus and ultimate strength of trabecular bone in tension are 0-2.5GPa and 3-20MPa, respectively and in compression are 0.1-3GPa and 1.5-50MPa, respectively [4].

Bones structural integrity is continuously maintained by a process called bone remodeling [5]. Osteoblast-bone forming cells and osteoclast-bone resorbing cells assemble into Basic Multi-cellular Units (BMUs) and the bone is completely remodeled. During bone remodeling process, some osteoblasts become encased in the matrix they produce to become osteocytes which are believed to play an important role in mechanotransduction. Whereas, remaining osteoblasts either undergo apoptosis or become bone lining cells [5].

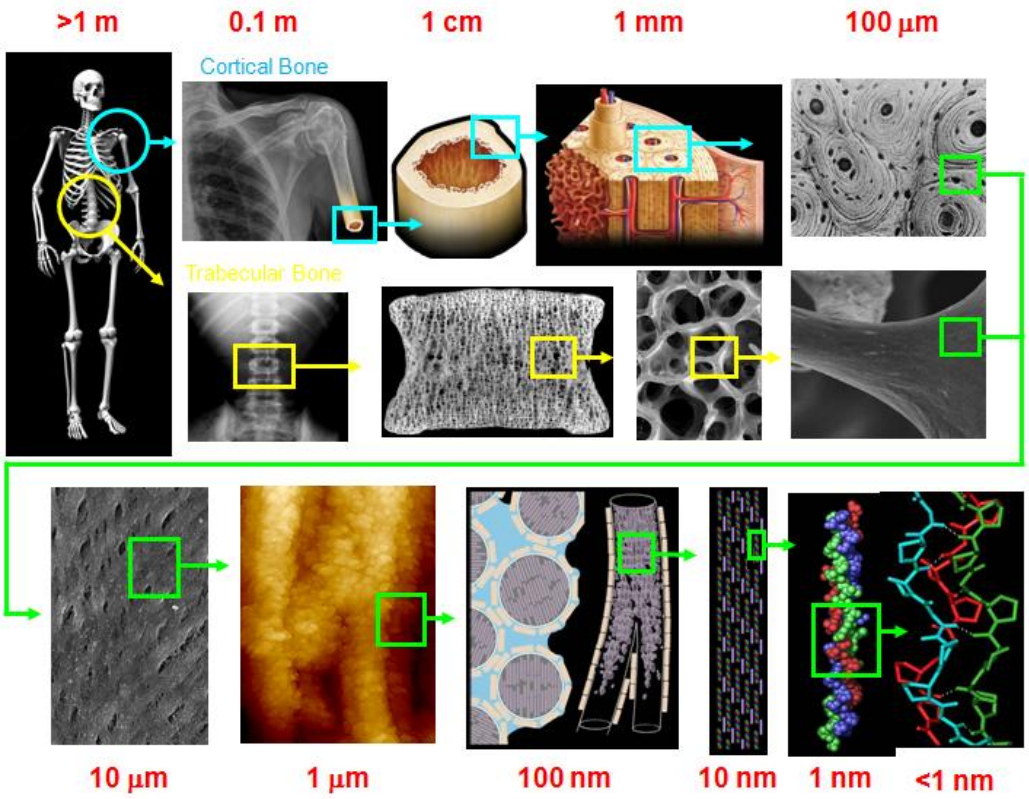

Figure 1. Shows complex hierarchical structure of the bone tissue from its smallest scale feature, <1nm, to its largest scale feature, >1m [2]

Individual collagen molecules deform by stretching and unwinding due to entropic and energetic mechanisms that involve hydrogen bond breaking. In collagen fibrils, stretching competes with intermolecular sliding resulting in both weak and strong bond breakage between tropocollagen molecules. These sliding motions allow bone to sustain large plastic strains and prevent bone from undergoing catastrophic brittle failure [2]. The presence of hydroxyapatite in bone is essential for its stiffness. Continuous glide between tropocollagen molecules and hydroxyapatite crystals at hydroxyapatite-tropocollagen interface dissipates tremendous amount of energy once the material starts to yield under stresses.

At larger submicron scale, the relative motion of mineralized collagen fibrils is the origin of post yield deformation in bone [2]. This motion is resisted by the interfibrillar matrix of primarily noncollagenous proteins such as osteopontin and sialoproteins in an aqueous environment [6]. This resistance is also an important mechanism of energy dissipation. In the vicinity of a crack, this slipping leads to the formation of a plastic zone where elastically stored energy can be dissipated to oppose further spreading of the fracture.

Microcracks are typical in bone, often formed as a result of daily activities such as walking or running. Microdamage normally forms at the weak interfaces which are important for many toughening mechanisms in bone such as crack bridging, crack deflection and un-cracked ligament bridging [2]. In crack bridging, intact collagen fibers can bridge a developing crack and carry the load that would otherwise be used to propagate the crack into the material. Crack deflection occurs when propagating crack encounters an interface and deviates from the direction of the maximum tensile stress. In un-cracked ligament bridging, an unbroken region is formed between a primary growing crack and other initiated ahead of it, which can carry significant load.

Factors besides bone size, mass, and density are important to the changes that make the bone tissue more susceptible to fracture with age [7-9]. One major factor that changes or deteriorates with age is bone strength. The clinical consequence of this deterioration is bone fracture, which contributes to the morbidity and mortality of osteoporosis patients [10]. Bone strength can be thought of as the integration of bone mass and bone quality.

Current techniques for clinical estimation of bone strength or susceptibility to fracture are based mainly on Bone Mineral Density (BMD) assessment [11]. These measurements are normally made using densitometry techniques such as Dual Energy X-ray Absorptiometry (DEXA). However, the sensitivity and specificity of such techniques are modest [11-12]. Moreover, these techniques do not provide complete information on strength/fracture due to their dependence on areal BMD measurement, which is different from engineering or apparent density. Furthermore, advanced bone imaging and analysis technologies such as QCT and pQCT promise better assessment of bone strength but depend on inaccurate assumptions about the tissue-level mechanical properties [13] and can involve high levels of radiation. There is clinical and laboratory evidence that in addition to BMD, the mechanical properties of bone tissue, specifically fracture toughness, play a crucial role in bone strength [14-16] and would serve as a useful predictor of bone fracture risk. However, available methods for direct estimate of this property clinically require invasive bone sampling [17].

Traditionally, measurement of the fracture toughness of bone using methods such as R-curve, J-integral and crack tip opening displacement (CTOD) involves large samples of bones, which obviates their use clinically. For instance, the resistance to extension of crack paths can be quantified, on machined and notched specimens, by resistance curve (R- curve) analysis [18-19] and using in situ observations and measurements in an environmental scanning electron microscope (ESEM) [20], respectively. However, crack growth toughness cannot be determined *in vivo* by employing such techniques.

In the past some attempts have been made to investigate fracture toughness of human bone clinically. For instance, in recent years a device called the 'Osteopenetrometer' was developed for intraoperative measurement of bone strength [21]. However, this device used a relatively large indenter tip geometry, over 2mm in diameter, that indented trabecular bone by distances on the order of 10mm at force of hundreds of Newton's by surgically exposing the bone [10]. Thus, it was highly invasive and proved to be inappropriate for clinical assessment. There have also been numerous previous evaluations of the toughness of human cortical bone [22-25] *ex vivo*; however, none of these emphasized the crack growth behavior in the cortical shell in the transverse direction [20], which is the situation in clinical fracture. In addition, many previous measurements of the toughness of mammalian cortical bones in situ have produced a single value of the toughness, for instance the fracture toughness K_c. However, this parameter does not necessarily include any contribution from the crack growth toughness [20] or extrinsic toughening mechanisms. Furthermore many of these evaluations, with few exceptions [26-27], were based on linear elastic fracture mechanics (LEFM) theory, which does not consider the contribution of plastic or inelastic deformations. There is a widely held assumption that bone tissue displays shear dominated plastic strain [28-29] as the stress-strain curve becomes non-linear at high stresses. However, whether bone displays true plastic strain in these conditions has yet to be established.

Indentation techniques for assessing toughness such as Vickers indentation fracture (VIF), cube corner indentation fracture (CCIF), Vickers crack opening displacement (VCOD) and the interface indentation fracture (IIF) tests [30-34] are attractive due to their simplicity and their potential to allow for characterization of both local and bulk properties. Unfortunately, such

techniques do not provide accurate fracture toughness values for many materials [35]. In addition, these techniques are inappropriate for measuring fracture toughness *in vivo* as they typically involve bulky instruments that often make their displacement measurements relative to a large, heavy, stabilized frame (Figure 2A).

Recent data suggest that a reference point indentation approach provides a localized measure that is related to fracture toughness [36] using a novel instrument (Figure 2B) that can be used both *ex vivo* and *in vivo*. The reference point indentation instrument [37-38] generates a novel measurement parameter called Indentation Distance Increase (IDI), which is related to fracture toughness and could possibly serve as a clinical indicator of fracture risk [36].

The reference point indenter consists of a cono-spherical test probe that is housed inside a reference probe and is pushed into the surface of a material in a cyclical manner, at a pre-determined force and frequency. The motion of the test probe during indentation is measured relative to the reference probe, which is stationary at the material surface. A schematic of the system illustrating the probe assembly, force generators and force/distance transducers is shown in Figure 2C. The reference probe is a modified hypodermic needle (22G; 710μm diameter) with blunted end and the test probe is a cono-spherical axisymmetric probe with 2.5μm tip radius and a 90^{o} conical end. Both probes are sharpened to minimize the lateral offset between their tips. The head unit is supported by a spring to reduce its weight and is held in place by a vertical slider, allowing only vertical movement. The instrument's control system supplies a modified triangular waveform to the force generator for the primary loading cycles used in the measurement [39]. The Indentation Distance Increase (IDI) is a novel parameter that the

reference point indentation instrument can measure. IDI is defined as the increase in the indentation distance in the last cycle relative to the first cycle (Figure 2D). It has been shown empirically that this parameter is related to the fracture toughness of whole bones [36]. IDI has been found to be consistently larger in bones that are known to be more brittle [36].

In the current research, we aim to evaluate the sensitivity of this reference point indentation instrument in situ to discriminate small known differences in bone brittleness and mechanical properties that exist between inbred mouse strains with genetically based differences in mineralization [29]. A/J mice, as compared to C57BL/6J (B6) mice, have significantly greater total femoral mineral content. In addition, C3H/HeJ (C3H) mice have an ash content intermediate to A/J and B6 [40]. C3H mice have a mineral-to-matrix ratio intermediate of A/J and B6, and cross-link maturity greater than both A/J and B6 [40]. Furthermore, A/J bones are more slender as compared to B6 and C3H which makes them mechanically weaker; however, this is compensated with increased mineral contents in order to improve stiffness.

We hypothesize that IDI could be used to detect differences in brittleness among these strains. We will also investigate local differences in mineralization at indentation site using microCT. In addition, we will analyze microdamage patterns beneath the indents and tissue microarchitecture, specifically, bone type and total void volume at the indented site, to characterize damage and to investigate any correlation between the void volume and IDI.

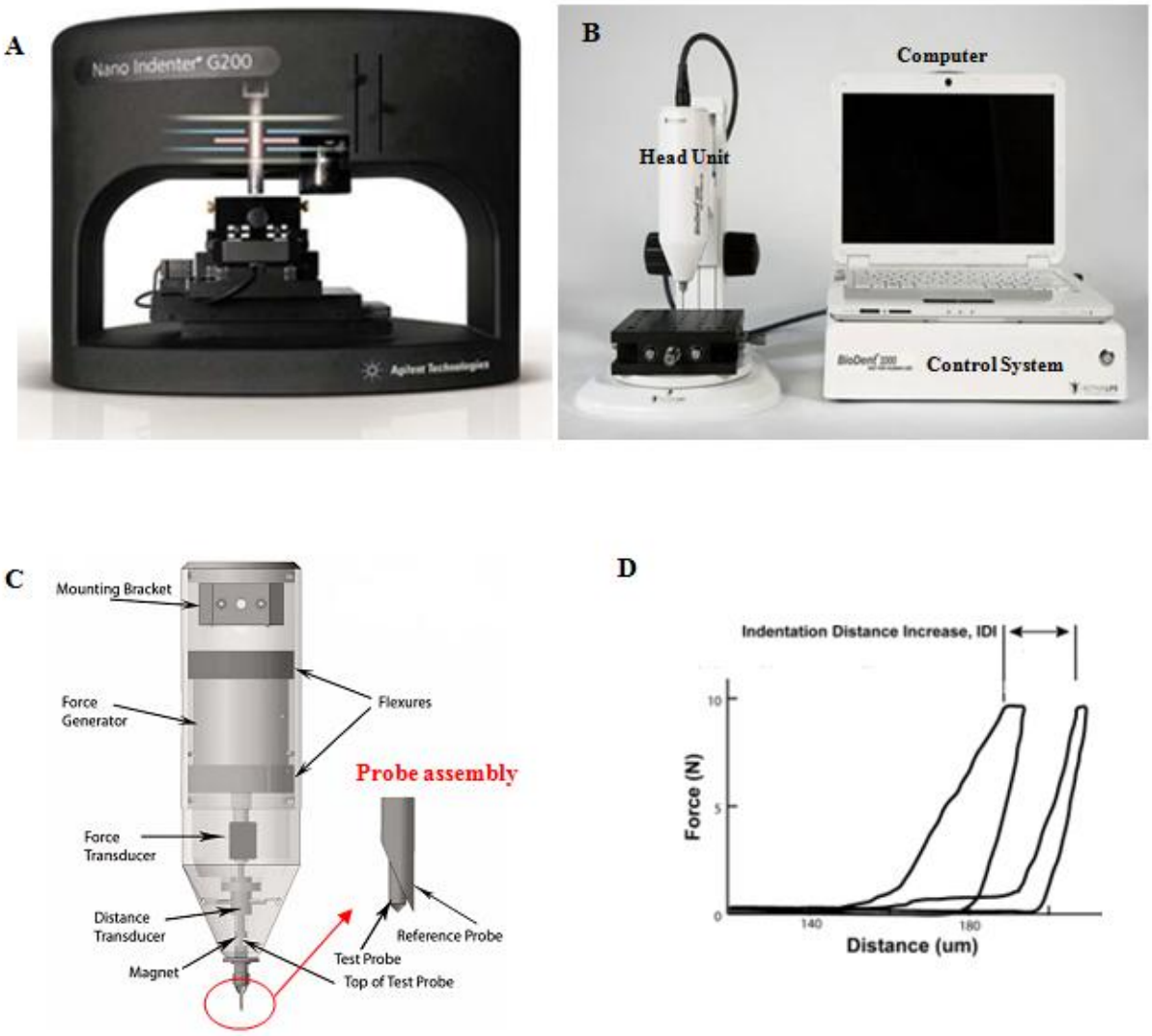

Figure 2. (A) Nanoindenter G200, a commercially available indentation testing device (www.google.com). (B) Reference Point Indentation instrument that measures Indentation Distance Increase (IDI) (www.activelifescientific.com). (C) [34] Head unit of the reference point indenter that provides housing for various elements that are illustrated. (D) [34] Force versus distance curves are used to quantify IDI.

2. Materials and methods

2.1 Sample preparation for mechanical testing

Three genetically distinct strains of mouse: A/J (AJ), C3H/HeJ (C3H) and C57Bl6 (B6) of same sex (female) and age (17 weeks) were used for indentation testing (n = 5/strain). All animals showed body weight as previously reported that is 25±3g. All animals were purchased from Jackson Laboratory (Boston), to avoid variability in the data due to diet and house-keeping factors. Animals were euthanized with CO_2 gas and left femora were excised. Femora were then wrapped in gauze soaked in PBS with 1mM $CaCl_2$ (25ml of $CaCl_2$ in 500ml PBS) and stored in -80^{o}C freezer until testing. Prior to mechanical testing, samples were removed from the -80 freezer and thawed out.

2.2 Reference point indentation testing

All testing was carried out using the reference point indentation instrument (Active Life Scientific Inc., Santa Barbara, CA). To achieve reproducible mechanical testing conditions a custom built specimen holder was used (Figure 3). The distal end of the sample was clamped to provide stability during testing and a metal rod was placed beneath the bone at the indentation site, to provide support and eliminate bending stresses. To prevent dehydration of the bone, the sample holder was fully submerged in PBS with 1mM $CaCl_2$ during indentation testing. The testing protocol that was developed for testing mouse femora involved applying a maximum load of approximately 7N, for 20 cycles at a frequency of 1Hz. This maximum load was selected to avoid technical limitations or constraints of the reference point indentation instrument. Careful alignment of the indenter on the bone was essential for maintaining correct touchdown distance.

The touchdown distance is the distance that the test probe travels from its resting position to the surface of the specimen. This distance depends on the specimen surface flatness and the distance between the tip of the test probe and the tip of the reference probe.

Two indentation measurements were made on the posterior diaphyseal surface of each femur, separated by an interval of approximately 500 μm. The orientation of the sample was such that the bevel of the reference probe rested perpendicular with a tolerance of ± 2 degrees on the bone surface (Figure 3). Prior to indenting bone samples, approximately three indents were performed on the cast acrylic samples using same protocol for system stabilization. The IDI from each test was collected using the Osteoprobe II manufacturer software.

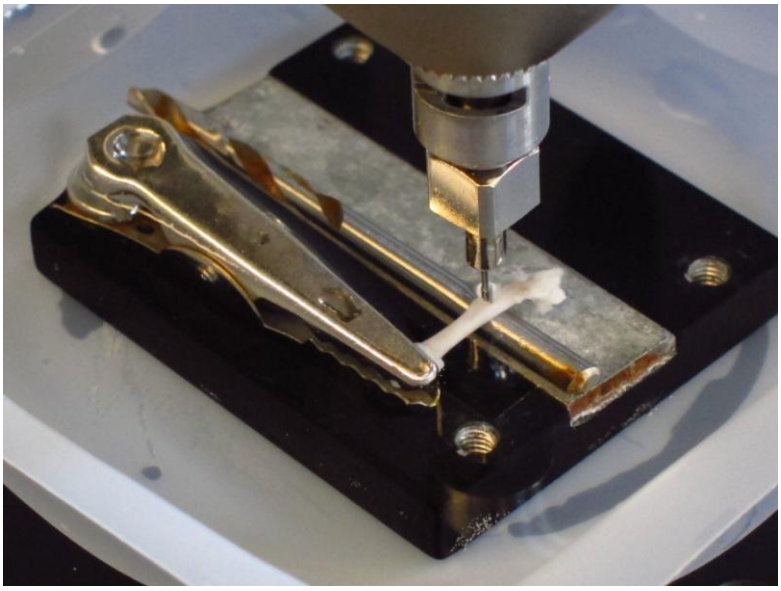

Figure 3. The distal end of the femur is clamped to provide stability for testing and the probe asseembly is lowered to rest perpendicularly on the bone, which is submerged in PBS with 1mM $CaCl_2$. A metallic rod is placed under bone such that it is aligned with the probe assembly.

2.3 Sample preparation for microdamage analysis; Histology

Indented samples were fixed in 10% zinc buffered formalin (Anatech Ltd., MI) for approximately two days in order to prevent tissue autolysis. Samples were then bulk stained in basic fuchsin dye for one week. Basic fuchsin dye was prepared by following bulk stain protocol for microdamage in bone. Briefly, stock solution was prepared by dissolving 10g of basic fuchsin (Fisher Chemicals, NJ) powder in l000ml of 99.95% (200 Proof) ethanol (Acros, NJ). Then, 80% and 90% fuchsin dyes were prepared from the stock solution to allow for gradual dehydration and staining of tissues. Samples were further dehydrated using Ethylene Glycol Mono-ethyl Ether (EGME), 2-Propanol and Petroleum Ether (all reagents from Fisher Chemicals, NJ) for 24 hours. Once fully dehydrated, samples were processed for plastic embedding. This process involves successively infiltration of MMA I (monomer), MMA II and MMA III (containing benzyl peroxide catalyst) for 24 hours. Then samples were embedded in a partly polymerized PMMA and were then incubated (Thermo Fisher Scientific, NJ) at 37^{o}C for complete polymerization. Samples were then cut into rectangular block (Figure 4) using a band saw (Marmed Inc., OH). These blocks were sequentially polished using silicon carbide papers (order: 600G, 800G and 1200G) (Buehler, IL) to expose the indented site.

2.3.1 Fluorescence and Scanning Electron Microscopy

Polished bone specimens were evaluated using fluorescence microscopy (Zeiss Inc., USA) to characterize damaged tissue. While damage patterns were visible using this approach, scanning electron (secondary electron) microscopy (SEM) was also used to examine particular features at higher magnification. In preparation for SEM, all the samples were placed in physical vapor

deposition chamber (Cressington Coating System 308R, USA) for gold (Au) coating. The deposition chamber was pressurized to 10^{-7}mbar to prevent the ionization of air. After the chamber was fully pressurized, evaporation supply or current source was turned on to melt the gold wire. This allowed a 32nm thick gold layer deposition on the samples. The layer thickness was monitored using a Cressington thickness monitor that utilizes gold density to calculate the thickness. After coating, samples were removed and imaged using a scanning electron microscope (Zeiss Inc., EVO40, USA) with secondary electron detector. The working distance was 8.5mm, the sample plane was oriented perpendicular to the electron beam incidence, and 9.5kV accelerating voltage was employed with a 2.6A operating current. The images were captured at different resolutions and magnifications (10-2µm Resolution; ~300X - ~1.4KX Magnification). SmartSEM software (Zeiss Inc., USA) was used for microdamage analysis. The contrast and brightness levels were adjusted so that electron images would be optimized for all samples.

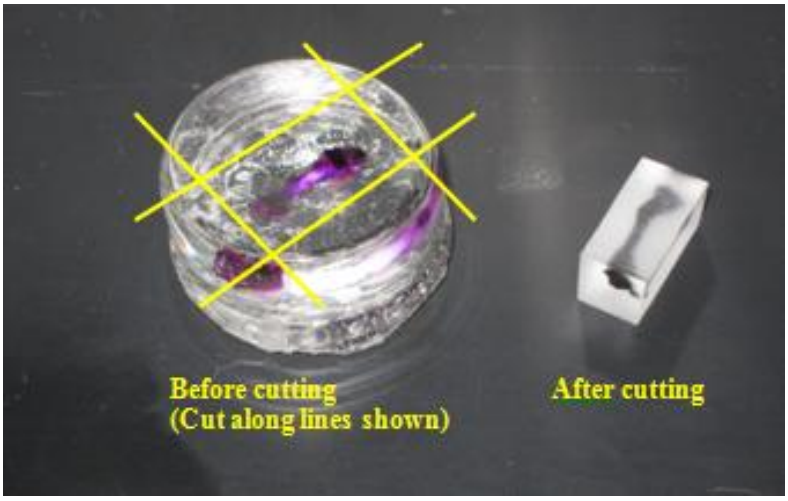

Figure 4. Rectangular block for sequential polishing was obtained by cutting fully polymerized PMMA.

2.4 Tissue Mineral Density (TMD) analysis

In a separate experiment, using different animals, 12 mice (AJ, C3H and B6, n=4/strain) of same sex (female) and age (17 weeks) were used for local Tissue Mineral Density (TMD) analysis. Animals were euthanized and femora were excised as before. Bones were fixed in 10% phosphate buffered formalin (Fisher Chemicals, NJ). Samples were then scanned using a microCT scanner (Skyscan, Belgium) with specific scan properties (Resolution = 6.7µm; Magnification = 26.9µm; Height of the stage on which the sample was mounted = 48mm; Camera = small (2000pixels); Filter = Al 0.5mm; Source Voltage = 100kV).

Femora were placed in an upright position in the scanning bone holder which was designed to accommodate thirteen mice bones and/or hydroxyapatite (HA) phantoms. Bones were immersed in PBS during scanning to prevent drying, thereby eliminating movement artifacts due to shrinkage. Also, caution was taken to eliminate bubbles from the solution in order to maintain stability of the bones while scanning. Two HA phantom rods (~1.5mm Diameter; ~5mm length), closely matching the cross-sectional thickness of a mouse femur were also scanned for density calibration. This allowed the HU (Hounsfield Unit) density value to be calibrated simultaneously. Streak artifacts that normally occur when high density samples are surrounded by low density medium were eliminated by scanning over 360 degrees. Therefore, the accuracy of the density measurements was optimized.

After scanning, the resultant images were reconstructed using NRecon software (SKYSCAN, Belgium). Optimum reconstruction parameters were selected (Post alignment = 0.5; Beam

hardening = 40; Ring reduction = 12; Smoothing = 1) for optimized images. Specially, beam hardening was optimized using aluminum filter, and the applied voltage was minimized to allow adequate transmission through the samples. Correct beam hardening was essential for control of the wide X-ray energy distribution from the source and selective removal of low energy photons as the beam passes through the sample. All the reconstruction parameters selected were identically applied to bone samples and HA phantoms, as all samples were scanned simultaneously.

After scanning, reconstruction and calibration of the HA phantoms, HU and TMD calibration was carried out using CT-Analyzer (CTAn) (Skyscan, Belgium) software. A circular region of interest (ROI) of water excluding the surface layer was selected. This surface layer was excluded in case of any small uncorrected beam-hardening or bubbles near the surface. This was made into a volume of interest (VOI) over a number of layers of water. The mean (total) density as grey level for the water VOI was found out to be 21.74897. In HU calibration, the grey and HU values were linked appropriately. Grey of 0 corresponded to HU of -1000, and grey of 21.74897 corresponded to HU of 0; this calibration was implemented. The calibration was re-normalized by the system and the equivalent HU values represented the minimum and maximum (black and white) grey values of 0 and 255. The HU value corresponding to the maximum density grey value of 255 was 10725. Now that HU was calibrated, recorded calibrated HU density values for HA phantoms were used (0.25g/cm^3 and 0.75g/cm^3). These two calibrated HU values were the basis for implementing the TMD calibration. Finally the restricted mean value for density of cortical bone was recorded. Only the region of cortical bone along lateral trochantor was analyzed for TMD, as this corresponds to the area of indentation.

2.5 Tissue microarchitecture analysis

To verify that IDI is a function of tissue composition and not the bone porosity, tissue microarchitecture was analyzed. After scanning, bones were transferred back to 10% phosphate buffered formalin. Samples were then embedded in PMMA using the same method described in Section 2.3. Rectangular blocks were cut transversely into 100 micron thin sections using a saw microtome (diamond blade; 250 micron blade thickness) (Leica Microsystems, USA). Sections were then polished using silicon carbide papers (order: 600G, 800G and 1200G) to reduce thickness to approximately 70-80 microns. Sections were then sonicated to remove debris, rinsed with p-Xylene (Fisher Chemicals, NJ) and mounted on glass slide using Eukitt mounting medium (Electron Microscopy Sciences, PA). They were then analyzed for microarchitecture, in particular, bone type and void density.

2.5.1 Bright field microscopy and 3D imaging (ApoTome) technique

Permanently mounted bone sections were analyzed under bright field microscopy using DIC camera settings and 20X magnification to investigate the bone type (lamellar vs. non-lamellar). In order to quantify the void volume, a novel 3D optical sectioning technique was used (ApoTome, Zeiss Inc, USA). The basic concept behind this approach is the use of an evenly spaced grid in the aperture plane that acts like a mask through which the specimen is illuminated. The grid is inserted into the light path of the microscope and uses the epi-illuminator lens system to project a shadow of the grid lines into sharp focus, superimposed on the specimen, in the objective focal plane. Initially, five slices or layers from each bone section (2 sections/bone; 3 bones /group) were imaged in different planes in Z-direction, with an optimal interval distance of

0.6μm. These optically imaged slices were then combined by the ApoTome system to form a single 2D optimized image. This image was used to quantify the void volume. Each osteocyte lacuna had an approximate elliptical shape therefore its major and minor axes were measured. To obtain the void volume, osteocyte lacunae were considered to be ellipsoidal therefore their void volume was calculated by assuming the third dimension of the "ellipsoid" equivalent to the minor axis. Furthermore, the total numbers of osteocyte lacunae in a prescribed area of the posterior diaphyseal region were counted to measure the numerical lacunar density.

2.6. Statistical analysis

Student's *t*-test was used to find the statistical difference in IDI between AJ and C3H. B6 had single IDI value therefore it was eliminated from the statistical analysis. Student's *t*-test test was used because the test statistics followed the normal distribution. The non-parametric Kruskal-Wallis test was performed with a Games-Howell and Tukey HSD post hoc analysis using SPSS 16.0 software to find the statistical difference in local mineralization between the three groups and to find the differences in the lacunar void volume between the three groups.

3. Results

3.1 Mechanical (Reference point indentation) testing

IDI was highest in AJ followed by C3H and B6 (Figure 5). Certain indents in B6 mice led to buckling of the cortex and bone failure due to inherently thin cortices (Figure 6). However, one successful indent was obtained from an animal with sufficiently thick cortex. Differences in IDI between AJ and C3H reached statistical significance ($p < 0.05$).

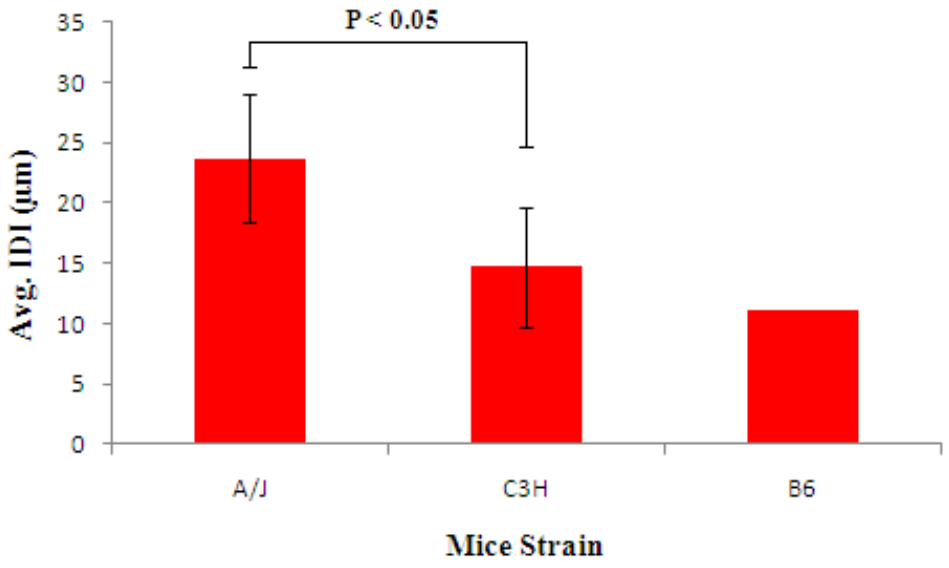

Figure 5. Indentation Distance Increase (IDI) for the three different mouse strains: AJ, C3H and B6. Figure displays mean ± SD for the A/J and C3H. For the B6 bone however, just one successful indent was obtained therefore there is no mean ± SD.

3.2 Fluorescence Microscopy Observations

These data showed that all indents for AJ and C3H bones were sharp and well delineated (Figures 7A & 7B). Many B6 femora showed extensive delamination due to thin cortex (Figure 7C); however, sharp indents were obtained in cases where cortices were sufficiently thick (Figure 7D). Qualitative analysis showed characteristic dark regions beneath the indents in AJ and C3H bones (Figures 7A & 7B) and that the reference probe produced creep effect due to its

constant loading during testing (Figure 7A). However, this effect did not interfere with IDI data in any of the bones due to sufficient (165μm) lateral offset. An additional qualitative observation from these tests was the presence of 'pile-up' in the vicinity of the indentation that is consistent with test sites from traditional indentation procedures (Figure 7D).

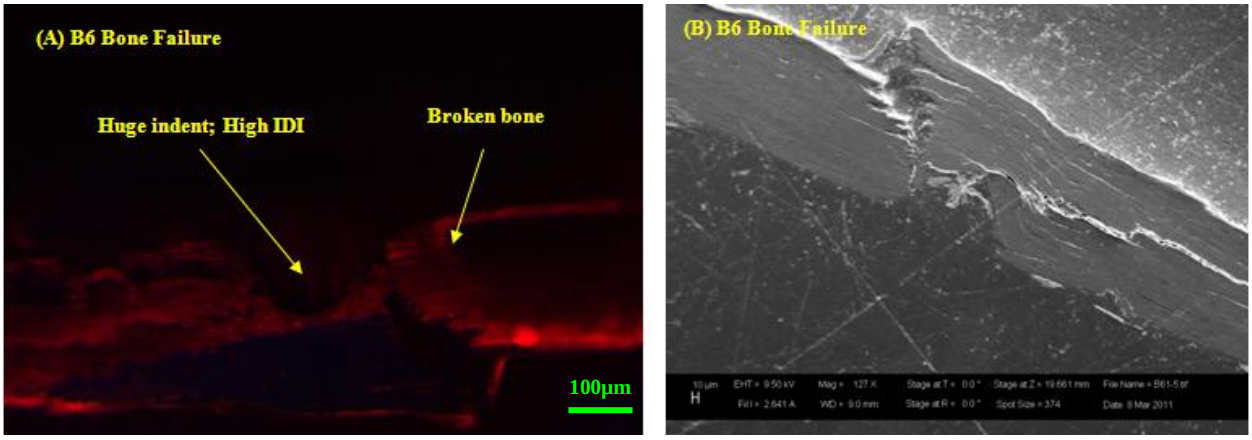

Figure 6. (A) Fluorescence image of a broken B6 bone. (B) SEM image of a broken B6 bone. Bone failure resulted in higher IDI values. Such IDI values were considered an error and were excluded.

3.3 Scanning Electron Microscopy Observations

In all bones a single or several small cracks formed under the indenter tip (Figures 8B & 8E). These cracks initiated in the transverse direction and immediately blunted by diverting into the longitudinal direction. Other toughening mechanisms were observed such as un-cracked ligament bridging in C3H bones (Figure 8C & 8D). Several cracks in the longitudinal direction were observed approximately in the middle of the cortex in AJ bones (Figure 8A). Parallel cracks due to buckling of the cortex or delamination were visible in B6 bones (Figure 8E).

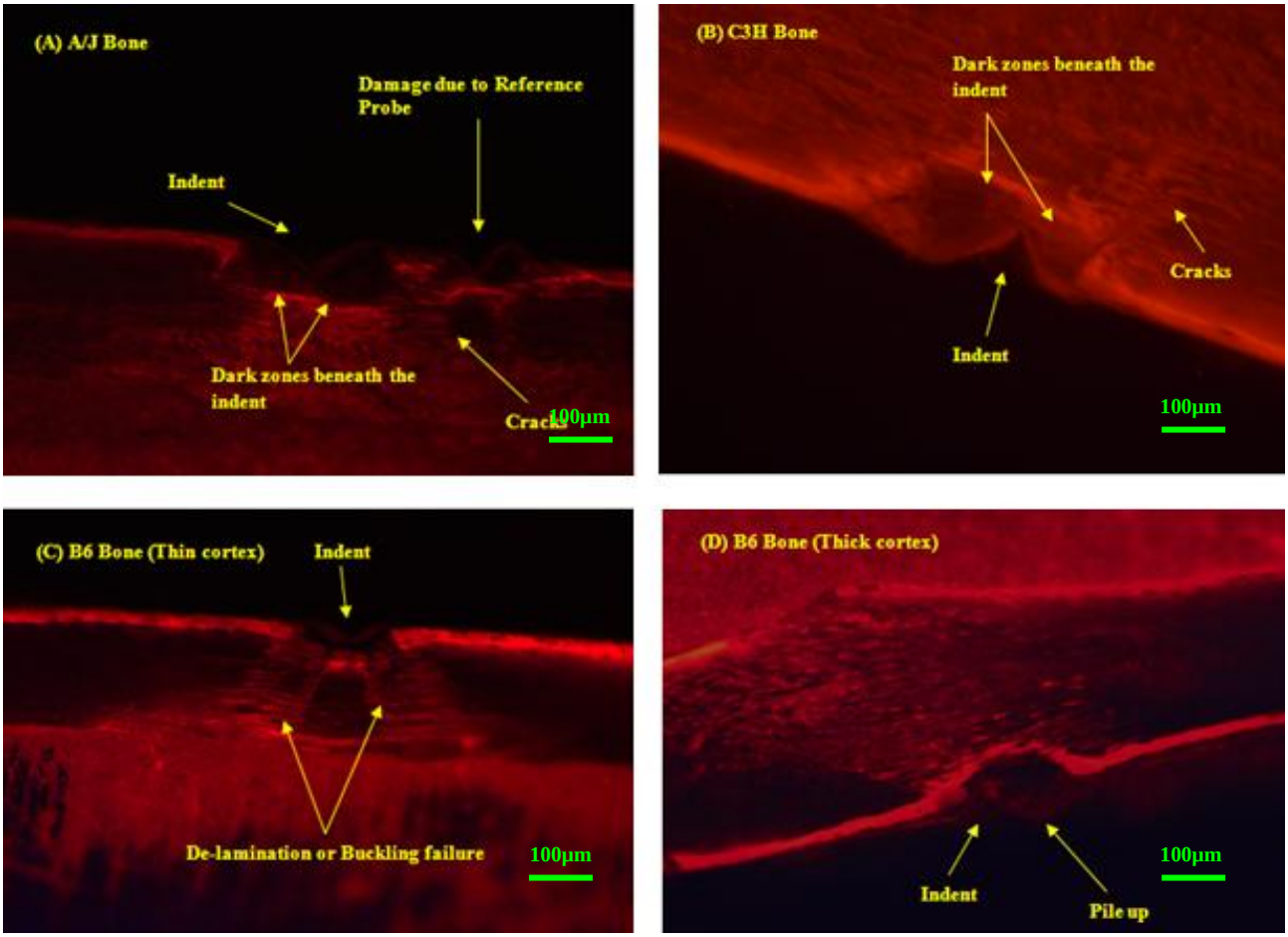

Figure 7. Panels (A) & (B) sharp and delineated indent in AJ and C3H bones; dark regions appear beneath the indent. Also in (A), creep effect can be seen due to constant loading of the reference probe. Panels (C) & (D) indent in thin and thick B6 cortex, respectively (C) delamination within the cortex (D) sharp indent; pile up is also visible.

3.4 Tissue Mineral Density (TMD) analysis

Local TMD was analyzed at the indentation site using microCT. TMD was highest in AJ followed by C3H and B6 (Figure 9). Statistical analysis showed significant differences between the groups ($p < 0.010$). Further statistical analysis using multiple comparison tests also showed significant differences between the groups (Appendix A).

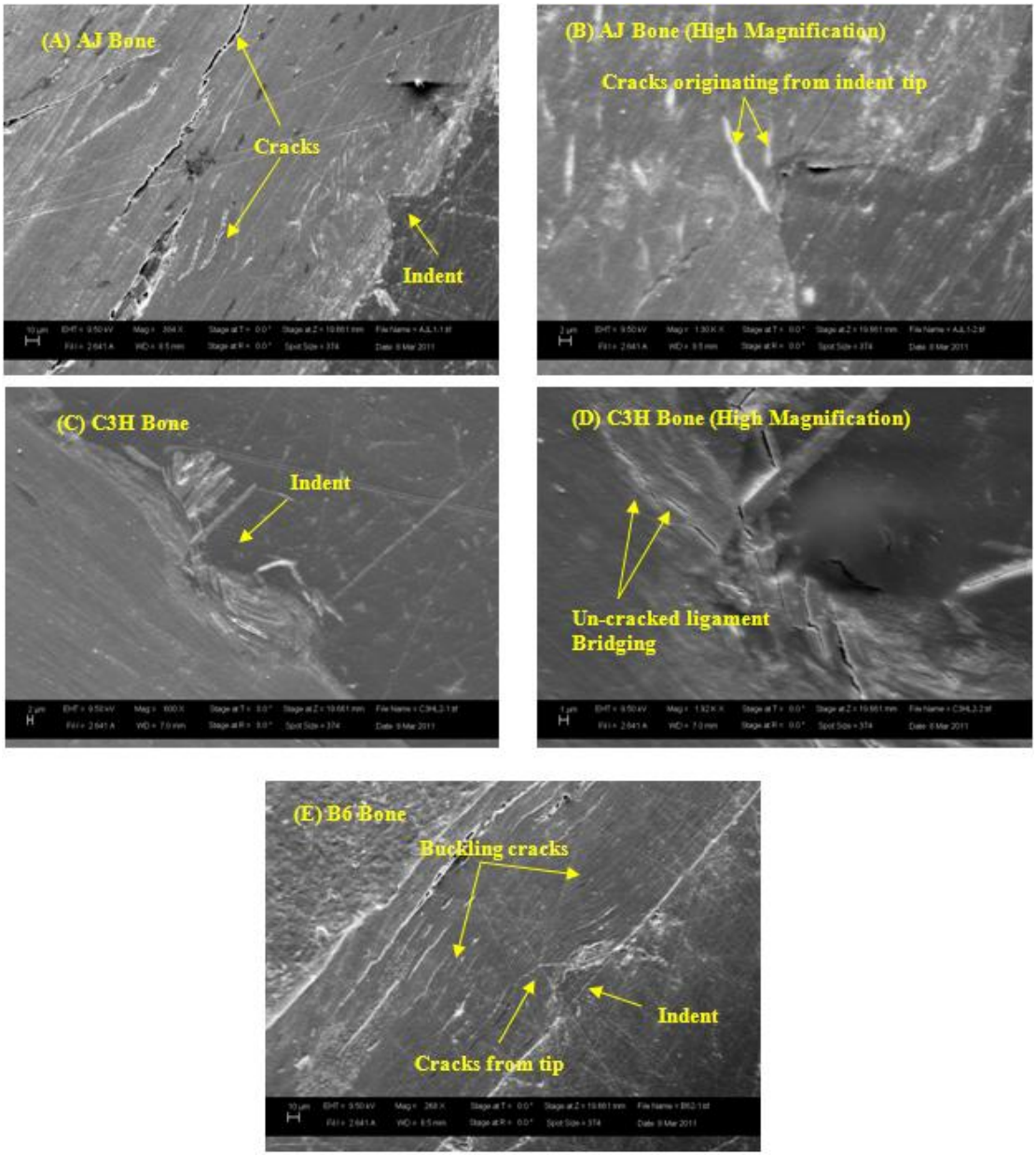

Figure 8. (A) Indent and cracks in the longitudinal direction, approximately in the middle of the cortex in AJ bone. (B) Shows same indent at higher magnification, clearly showing cracks originating from the tip. (C) Indent in C3H bone. (D) Shows same indent at higher magnification, clearly showing un-cracked ligament bridging. (E) Indent and cracks due to buckling in B6 bone.

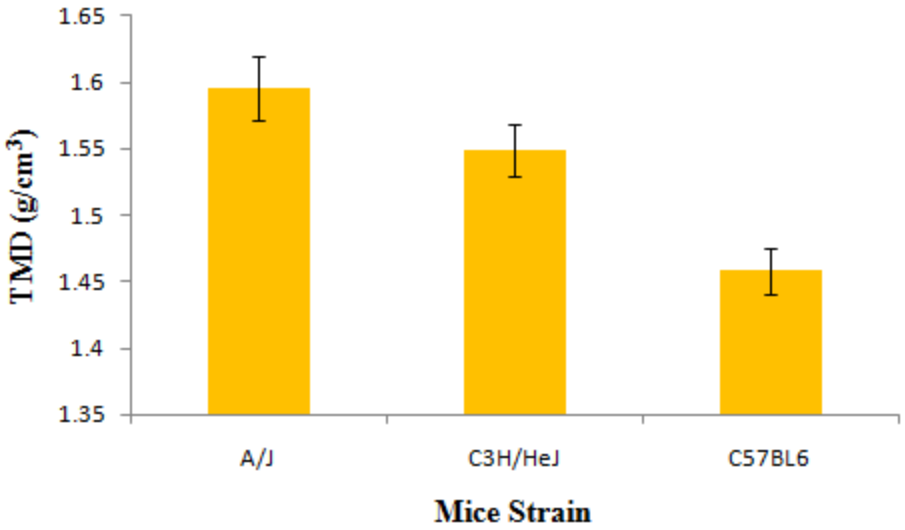

Figure 9. Tissue Mineral Density (TMD) was highest in AJ followed by C3H and B6. Statistically significant difference was found between the three groups. Figure displays mean ± SD for the A/J, C3H and B6.

3.5 Tissue Microarchitecture analysis (Void Volume)

Optical sectioning analysis (ApoTome) showed that in a given indented area (~ 200 x 95 μm^2), the lacunar density was highest in B6 followed by AJ and C3H (Figure 10; Table 1). The void volume was lower in AJ as compared to B6 and C3H (Figure 11); however, there was no significant difference in the lacunar void volume between the three groups ($P < 0.231$). Further statistical analysis using multiple comparison tests also showed no significant differences between the groups (Appendix A).

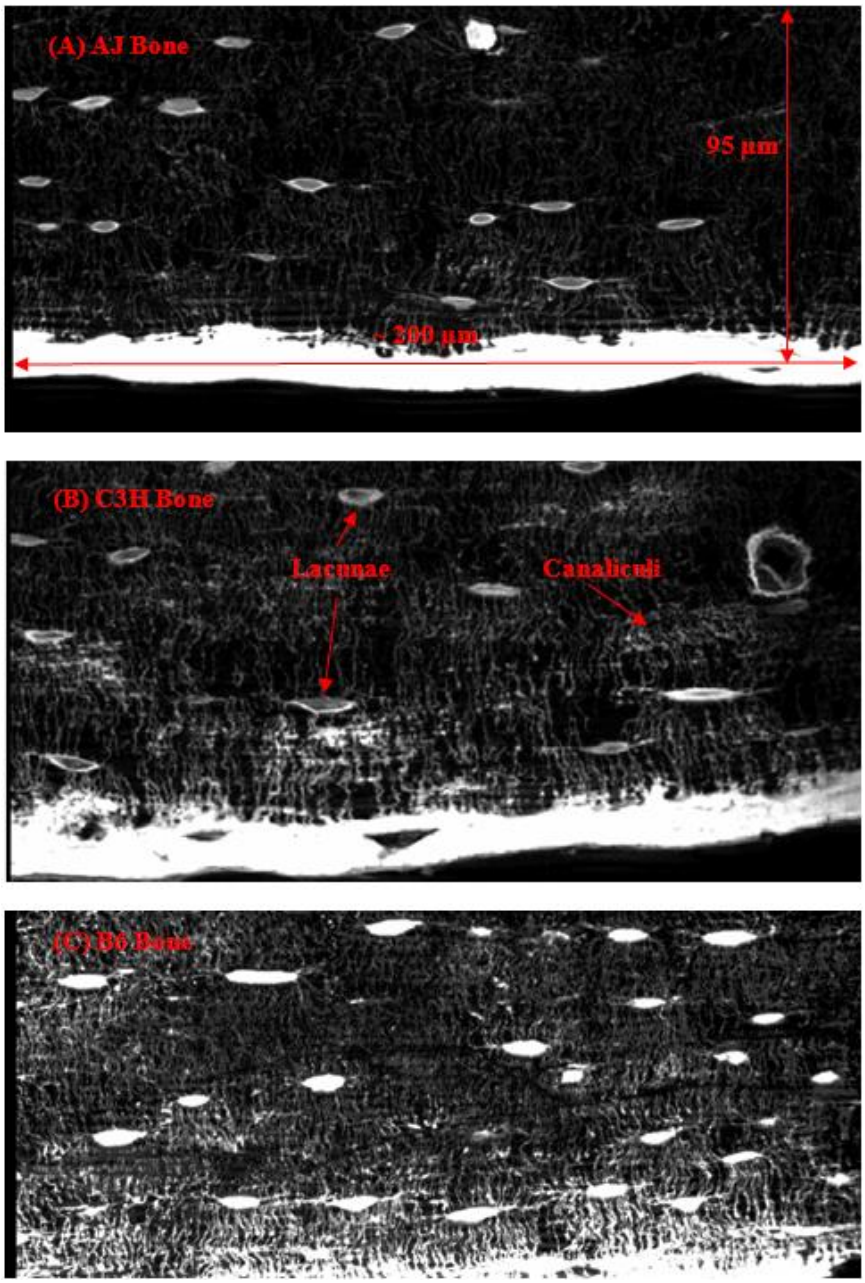

Figure 10. (A) Lacunar density in a given area in AJ bones obtained via ApoTome microscopy. Similarly, panels (B) and (C) show lacunar density in C3H and B6 bones, respectively.

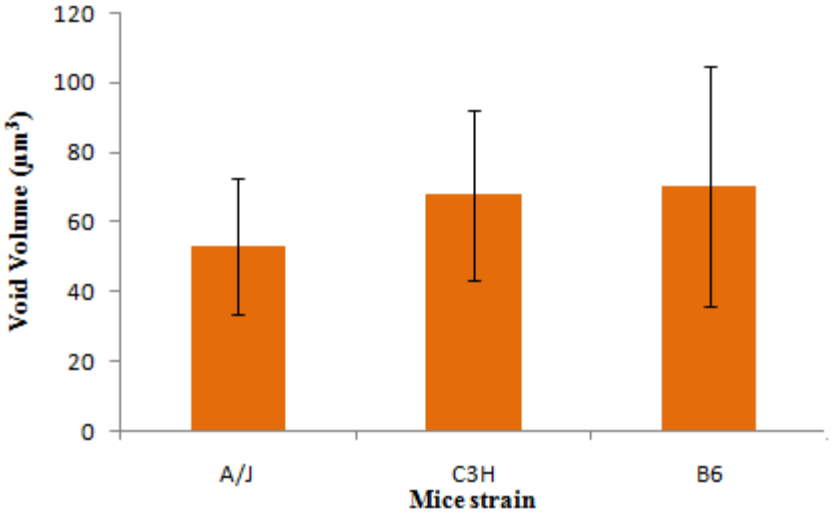

Figure 11. Shows lacunar void volume in AJ, C3H and B6. Figure also displays mean ± SD for the A/J, C3H and B6.

Strain	Lacunar numerical density (# / mm^2)	Average Major axis (µm)	Average Minor axis (µm)	Average void volume (µm^3) $P < 0.231$
AJ	842	11.57	2.91	53.16
C3H	578	13.35	3.05	67.70
B6	1100	12.92	3.15	70.35

Table 1. Summarizes the quantification of the lacunar void volume in AJ, C3H and B6.

3.6 Tissue Microarchitecture analysis (Bone type)

Bright field microscopy showed that B6 mouse had lamellar bone throughout the cortex (Figure 12C) whereas measurements in AJ and C3H bones revealed, part of the cortex approximately 100µm from the periosteum in AJ and approximately 200 µm from the periosteum in C3H, was lamellar bone and the remaining cortex was non-lamellar bone (Figures 12A & 12B).

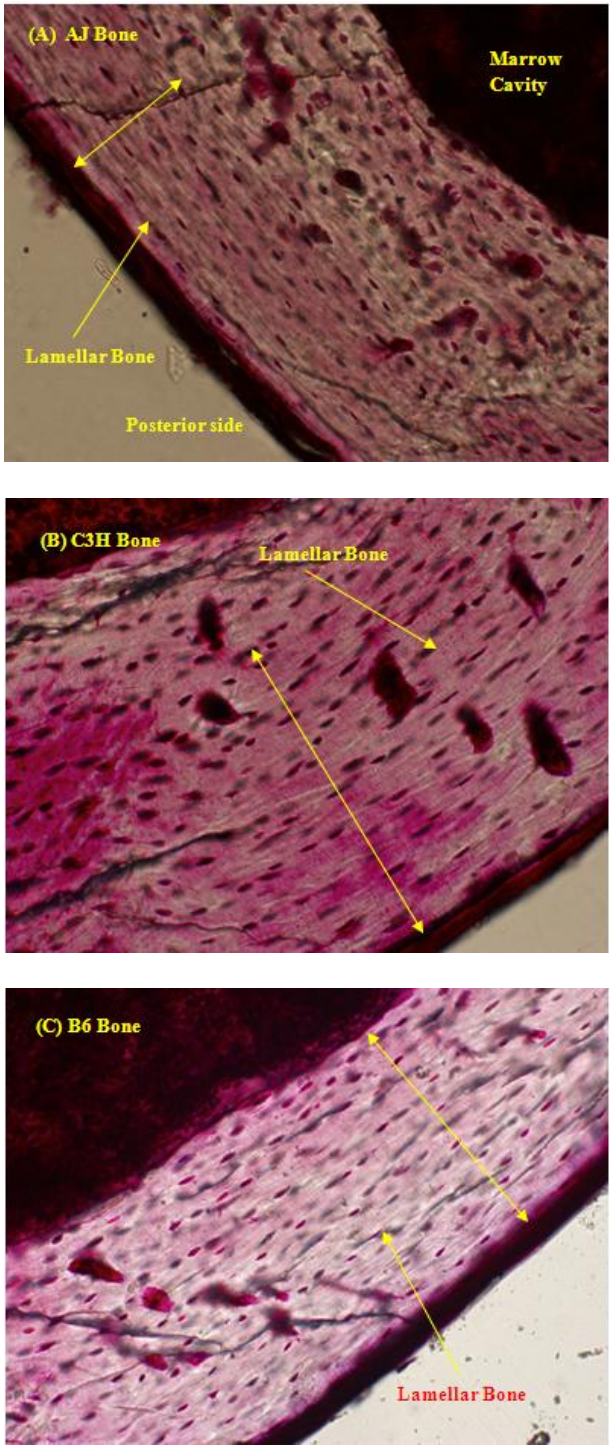

Figure 12. Microstructure of mouse cortices showing (shown by double head arrow) (A) 100 µm thick layer of lamellar bone in AJ mouse. (B) Approximately 200 µm thick layer of lamellar bone in C3H mouse. (C) Full cortex of lamellar bone in B6 mice.

4. Discussion

In these studies we describe the sensitivity of a novel reference point indenter that performs microindentation testing of whole mouse bone. Our system measures a novel parameter called Indentation Distance Increase (IDI). We measured this parameter in three separate strains of mice that are known to have genetically based differences in mineralization. We hypothesized that IDI could be used to detect differences in brittleness among these strains. IDI was found to be highest in AJ followed by C3H and B6. These data precisely parallel previously reported phenotypes for bone brittleness, where AJ are the most brittle, B6 are the least brittle and C3H were in between [29,40]. In addition, our results are also consistent with previously reported experimental results in which IDI for fresh bovine femoral bones (considered to be 'less brittle') were lower than the IDI for irradiated bovine femoral bones (considered to be 'more brittle', as a result of irradiation). Furthermore, these data are also in agreement with clinical findings for IDI in humans where aged female bone (female, 79 years) displayed higher IDI than young humans (female, 17 years) [40].

We have shown that bone tissue mechanical properties, specifically toughness as quantified by the IDI, was significantly different between AJ and C3H mice. Bone tissue from these two strains has been shown to have approximately 2-2.5% difference in the degree of mineralization [40]. Also, our data suggest that the reference point indentation is a suitable and sufficiently sensitive method for detecting differences in brittleness as a result of small known differences in mineralization. Therefore, the reference point indenter may have important clinical implications in the assessment of fracture risk clinically.

Indents were sharp and well delineated in all bones. The indent profile in all bones was consistent with previous reports in the literature for conical indenters in non-biological material [41]. Normally, axisymmetric indenters, such as conical, spherical or cylindrical indenters, induce cone cracks; however, no cone cracks were observed beneath the indent site in these studies. This may be explained because their visibility was compromised by dark regions beneath the indents. Therefore, whether or not cone cracks really exist for cone-spherical geometries in biological materials becomes a question to be investigated in future with refined visualization techniques.

Cracks were observed below the dark regions in AJ and C3H bones (Figures 7A & 7B). These cracks can be referred to as Hertzian cone cracks as they project radially down through the cortex from the site of loading. Lawn et al. have investigated cone cracks developing from the free surface in spherical indentation [42-45]. Here, the dark regions are formed probably due to compaction of tissue leading to poor penetration of basic fuchsin in AJ and C3H bones. This tissue compaction may have occurred probably due to collapse of the lacunar void space during indentation. This phenomenon caused a solid volume of collapsed material with a spherical profile to form. This volume may behave like a "spherical indenter" and generate Hertzian like cracks in AJ and C3H bones (Figures 7A & 7B). Interestingly, the fracture began its growth at the contact of these dark regions (Figures 7A & 7B). We suspect that these cracks run around the contact area in a uniform stress field, following the circular stress trajectories therefore, producing Hertzian like effect. In B6 bones with thin cortices Hertzian like cracks were not seen, this was most likely because the delaminating and buckling effects dominate this type of crack formation in these bones. However, other cracks that we have termed "buckling cracks" were

observed in these bones. The relationship between these cracks and Hertzian cone cracks has yet to be investigated.

Numerous thin walled B6 cortices failed during the process of indentation testing (Figure 6A & 6B). This suggests that the cortex of mouse bone has a minimum threshold that must be met in order to carry out this kind of indentation reliably. It may be the case that this wall thickness threshold for indent versus fracture would be different for lower loading forces; however, this could not be tested within the limits of prototype Biodent system used. In this study, bones with cortical thickness less then 210μm buckled or completely failed whereas, bones with thick cortex (> 210 μm) provided reproducible data.

Lacunar void volume was quantified in each of the strains in this study. The presence of dark regions in AJ and C3H confirms that the void lacunar volume collapse and form a sold mass that has spherical indenter like profile. Although, void volume for B6 was higher than AJ and C3H; no spherical indenter like profile was seen in these thin walled B6 cortices. There are two possible explanations for this observation (I) delamination created gaps between the individual lamina of the tissue and this resulted in sliding of the collapsed material into these gaps and (II) the differences between these tissue types is based solely upon matrix differences and is independent of local microstructure.

Our studies of bone type showed that B6 bones were lamellar throughout the cortex, with each lamina ‘glued’ to its neighbor by heavily phosphorylated non-collagenous proteins such as bone sialoproteins and osteopontin. During indention this “thin walled laminate” may have been more

susceptible to bending which could induce high shear stresses between the individual lamina. In this situation the non-collagen proteins would be forced to de-bond and produce the delamination effect. However, the bone structure was different in AJ and C3H (Figures 12A & 12B). Here, half or more than half of the bone was lamellar and the remaining contained “one thick ply” of woven like non-lamellar bone. This may have contributed significantly to the behavior of the material under load. Thicker cortices in AJ and C3H (> 220μm in AJ and > 280μm in C3H) as compared to B6 and presence of woven like structure in these (AJ and C3H) bones is assumed to increase their resistance to bending, thereby reducing bending stresses that are responsible for causing buckling.

The toughness of bone depends on how a crack propagates through the tissue and the relation between the crack and the bone matrix structure [46]. In bone many structural features provide toughening mechanisms that are active during crack growth. Therefore, fracture can be considered as a competition between intrinsic damage mechanisms that act ahead of the crack tip to promote cracking and extrinsic crack shielding mechanisms that act behind the tip to inhibit cracking [2, 47-48]. Some toughening mechanisms serve to limit the microstructural damage. For example, plasticity ahead of the crack is known to dissipate energy and locally reduce the stresses by blunting the crack tip (Figure 8B). Another toughening mechanism is the diversion of a crack from its initial path by the lamellar interfaces in bone; this can dramatically slow down the crack progression. Other toughening mechanisms such as un-cracked ligament bridging were observed in C3H bones (Figure 8D); an unbroken region was formed between a primary growing crack and other initiated ahead of it carried significant loads otherwise used to propagate the crack.

Local Tissue Mineral Density (TMD) data for all strains precisely parallel previously reported whole bone TMD in these strains and phenotypes for bone brittleness, where AJ are the most brittle, B6 are the least brittle and C3H were in between [29,40]. Importantly, these TMD data follow the same pattern as the IDI data in each strain. This strongly suggests that measurement of IDI by reference point indentation is a suitable and sufficiently sensitive method for detecting differences in brittleness as a result of small differences in mineralization. This may have important clinical implications in the future as the ability to carry out non-invasive fracture risk assessment of patients constitutes a significant advancement in the diagnosis of skeletal health.

References

1. Katz J.L, (1980) The structure and biomechanics of bone. Symp Soc Exp Biol 34:137-68.

2. Ritchie R.O, Buehler M.J, Hansma P, (2009) Plasticity and toughness in bone. Physics Today, 62(6): 41-46.

3. Rho J.Y and Zioupus P, (1998) Med. Eng. Phys, 20: 92

4. Information on mechanical properties of cortical and trabecular bone is obtained from the following website: http://www.orthoteers.co.uk/Nrujp~ij33lm/Orthbonemech.htm

5. Information on bone remodeling is obtained from the following website: http://www.elixirindustry.com/resource/osteoporosis/jilka.htm

6. Gupta H.S, et al (2006) Int. J. Fract., 139: 425

7. Schnitzler C.M, (1993) Bone Quality: a determinant for certain risk factors for bone fragility. Calcif Tissue Int, 53 (suppl 1): S27-S31.

8. Van der Meulen M.C, Jepsen K.J, Mikic B, (2001) Understanding bone strength: size is not everything. Bone, 29: 101-104.

9. Schuit S.C, Van der Klift M, Weel A.E, et al., (2004) Fracture incidences and association with bone mineral density in elderly men and women: the Rotterdam study. Bone, 34: 195-202.

10. Adolfo D.P, Roberto G, Xavier N, et al., (2010) Microindentation for in vivo measurement of bone tissue mechanical properties in humans. J Bone Miner Res, 25: 1877-1885.

11. Rivadeneira F, Zillikens M.C, et al., (2007) Femoral neck BMD is a strong predictor of hip fracture susceptibility in elderly men and women because it detects cortical bone instability: the Rotterdam study. J Bone Miner Res, 22: 1781-1790.

12. Yang L, Peel N, et al., (2009) Use of DXA based structural engineering models of the proximal femur to discriminate hip fracture. J Bone Miner Res, 24: 33-42.

13. Boutroy S, Rietbergen B.V, et al., (2008) Finite element analysis based on in vivo HR-pQCT images of the distal radius is associated with wrist fracture in post menopausal women. J Bone Miner Res, 23: 392-399.

14. Chavassieux P, Seeman E, et al., (2007) Insights into material and structural basis of bone fragility from the diseases associated with fractures: How determinants of the biomechanical properties of bone are compromised by disease. Endocrine Reviews, 28: 151-164.

15. Vashishth D, (2005) Age dependent biomechanical modifications in bone. Crit Rev Eukar Gene, 15: 343-357.

16. Currey J.D, (1979) Changes in impact energy absorption with age. J Biomech, 12: 459-469.

17. Seeman E, Delmas P.D, et al., (2006) Mechanisms of diseases- Bone quality- The material and structural basis of bone strength and fragility. New Engl J Med, 354: 2250-2261.

18. Nalla R.K, Kruzic J.J, Ritchie R.O, et al., (2005) Mechanistic aspects of fracture and R-curve behavior of human cortical bone. Biomaterials, 26: 217-231.

19. Vashishth D, Behiri J.C, Bonfield W, (1997) Crack growth resistance in cortical bone: Concept of microcrack toughening. J Biomech, 30: 763-769.

20. Koester K.J, Ager J.W, Ritchie R.O, (2008) The true toughness of human cortical bone measured with realistically short cracks. Nat mater, 7: 672-677.

21. Hvid I, Linde F, (2000) Penetration testing of bone using the Osteopenetrometer In: An Y.H, Draughn R.A, eds., Mechanical testing of bone and the bone-implant interface. Boca Raton, FL: CRC Press, 241-246.

22. Behiri J.C, Bonfield W, (1984) Fracture mechanics of bone- the effect of density, specimen thickness and crack velocity on longitudinal fracture. J Biomech, 17: 25-34.

23. Norman T.L, Vashishth D, Burr D.B, (1991) In advances in Bioengineering, ed. Vanerby, R. ASME, New York, 20: 361-364.

24. Zioupos P, Currey J.D, (1998) Changes in stiffness, strength and toughness of human cortical bone with age. Bone, 22: 57-66.

25. Wang X, Shen X, et al., (2002) Age related changes in the collagen network and toughness of bone. Bone, 31: 1-7.

26. Malik C.L, Stover S.M, et al., (2003) Equine cortical bone exhibits rising R-curve fracture mechanics. J Biomech, 36: 191-198.

27. Yan J, Mecholsky J, et al., (2007) How tough is bone? Application of elastic-plastic fracture mechanics to bone. Bone, 40: 479-484.

28. Taylor D, (2003) Fracture mechanics: How does bone break? Nat Mater, 2: 133-134.

29. Jepsen K.J, Pennington D.E, et al., (2001) Bone brittleness varies with genetic background in A/J and C57BL/6J inbred mice. J Bone Miner Res, 16: 1854-1862.

30. Anstis G.R, Chantikul P, Lawn B.R, et al., (1981) A critical evaluation of indentation techniques for measuring fracture toughness. I. Direct cracks measurements. J American Ceramic Society, 64(9): 533-538.

31. Pharr G.M, (1998) Measurement of mechanical properties by ultra low load indentation. Material Science and Engineering, A253 (1-2): 151-159.

32. Fett T, Kounga A.B, et al., (2004) Stresses and stress intensity factor from COD of Vickers indentation cracks. J Material Science, 39(6): 2219-2221.

33. Fett T, Njiwa A.B, et al., (2005) Crack opening displacements of Vickers indentation cracks. Engineering Fracture Mechanics, 72(5): 647-659.

34. Becher P.F, Sun E.Y, et al., (1996) Debonding of interfaces between beta-silicon nitride whiskers and Si-Al-Y oxynitride glasses. Acta Materialia, 44(10): 3881-3893.

35. Kruzic J.J, Kim D.K, et al., (2009) Indentation techniques for evaluating the fracture toughness of biomaterials and hard tissues. J Mechanical Behavior Of Biomedical Materials, 2: 384-395.

36. Randall C, Mathews P, et al., (2009) The bone diagnostic instrument III: Testing mouse femora. Rev Sci Instrum, 80: 065108-1- 3.

37. Hansma P, Turner J, et al., (2006) Bone diagnostic instrument. Rev Sci Instrum, 77: 075105-1-6.

38. Oliver W.C, Pharr G.M, (2004) Measurement of hardness and elastic modulus by phase transformation during the indentation of silicone. J Mater Res, 19(3).

39. Hansma P, Yu H, et al., (2009) Tissue Diagnostic instrument. Rev Sci Instrum, 80: 054303-1-6.

40. Hayden W.C, Spevak M, Boskey A, Jepsen K (2009) Genetic variation in mouse femoral tissue level mineral content underlies differences in whole bone mechanical properties. Cells Tissues Organs, 189: 237-240

41. Hansma P, Turner P, et al., (2008) The bone diagnostic instrument II: Indentation distance increase. Rev Sci Instrum, 79: 064303-1-8.

42. Yan J, Karlsson A.M, Chen X, (2007) On internal cone cracks induced by conical indentation in brittle materials. Engineering Fracture Mechanics, 74: 2535-2546.

43. Lawn B.R, (1998) Indentation of ceramics with spheres: A century of Hertz. J Am Ceram Soc, 81: 1977-1985.

44. Lawn B, Evans A, et al., (1980) Elastic-plastic indentation damage in ceramics- The median radial crack system. J Am Ceram Soc, 63: 574-581.

45. Lawn B.R, Fuller E.R, (1975) Equilibrium penny-like cracks in indentation fracture. J Mater Sci, 10: 2016-2020.

46. Lawn B.R, (1993) Fracture of brittle solids. Second edition, Cambridge University Press.

47. Ritchie R.O, Buehler M.J, Hansma P, (2009) Plasticity and toughness in bone. Physics Today, 62(6): 41-46.

48. Ritchie R.O, (1999) Mechanisms of fatigue-crack propagation in ductile and brittle solids. Int J Fract, 100: 55-83.

Appendix A

Multiple Comparison Tests (Tukey HSD & Games-Howell)

Dependent Variable: TMD			
	(I) GROUP	(J) GROUP	Sig.
Tukey HSD	1	2	**.036**
		3	**.000**
	2	1	**.036**
		3	**.001**
	3	1	**.000**
		2	**.001**
Games-Howell	1	2	**.073**
		3	**.001**
	2	1	**.073**
		3	**.001**
	3	1	**.001**
		2	**.001**

Depend. Variable: Void Volume			
	(I) GROUP	(J) GROUP	Sig.
Tukey HSD	1	2	**.369**
		3	**.241**
	2	1	**.369**
		3	**.959**
	3	1	**.241**
		2	**.959**
Games-Howell	1	2	**.234**
		3	**.267**
	2	1	**.234**
		3	**.966**
	3	1	**.267**
		2	**.966**

Kruskal-Wallis Test

Ranks			
	GROUP	N	Mean Rank
MINERAL	1	4	10.25
	2	4	6.75
	3	4	2.50
	Total	12	

Test Statistics	
	MINERAL
Chi-Square	9.269
df.	2
Sig.	**.010**

Ranks			
	GROUP	N	Mean Rank
VOLUME	1	16	20.38
	2	17	28.29
	3	17	27.53
	Total	50	

Test Statistics	
	VOLUME
Chi-Square	2.932
df.	2
Sig.	**.231**

Key:
Group 1 = A/J
Group 2 = C3H
Group 3 = B6

Acknowledgements

NIH
Grants AR41210 and AR60445

University of California, Santa Barbara
Dr. Paul Hansma

Active Life Scientific Inc.,
Alex Procter
Davis Brimer

Bone and Joint Lab; Biomedical Engineering Department at CCNY
Dr. Mitchell Schaffler (Principal Investigator)
Damien Lauder
Jelena Basta-Pljakic
Dr. Oran Kennedy
Dr. Luis Cardoso
Dr. Lane Gilchrist
Dr. Zhiyong Qiu

Chemical Engineering Department at CCNY
Dr. Ilona Kretzschmar
Sonia Mathew